Magnetic correlations in the magnetic topological insulator $(Cr, Sb)_2Te_3$

N.-J. Steinke,[1,2,*] S. L. Zhang,[3,†] P. J. Baker,[1] L. B. Duffy,[1,3] F. Kronast,[4] J. Krieger,[5,‡] Z. Salman,[5] T. Prokscha,[5] A. Suter,[5] S. Langridge,[1] G. van der Laan,[6] and T. Hesjedal[1,3,§]

[1]*ISIS, Rutherford Appleton Laboratory, Oxon OX11 0QX, England, United Kingdom*
[2]*Institut Laue-Langevin, 71 Avenue des Martyrs, 38000 Grenoble, France*
[3]*Department of Physics, Clarendon Laboratory, University of Oxford, Oxford OX1 3PU, England, United Kingdom*
[4]*Helmholtz-Zentrum Berlin für Materialien und Energie, Albert-Einstein-Strasse 15, 12489 Berlin, Germany*
[5]*Laboratory for Muon Spin Spectroscopy, Paul Scherrer Institute, CH-5232 Villigen PSI, Switzerland*
[6]*Diamond Light Source, Harwell Science and Innovation Campus, Didcot OX11 0DE, England, United Kingdom*

(Received 17 October 2022; revised 9 December 2022; accepted 13 December 2022; published 23 December 2022)

Chromium-doped Sb_2Te_3 is a magnetic topological insulator (MTI), which belongs to the $(Sb,Bi)_2(Se,Te)_3$ family. When doped with the transition metals V, Cr, and Mn this family displays long-range ferromagnetic order above liquid nitrogen temperature and is currently intensely explored for quantum device applications. Despite the large magnetic ordering temperature, the experimental observation of dissipationless electrical transport channels, i.e., the quantum anomalous Hall effect, is limited in these materials to temperatures below ≈2 K. Inhomogeneities in the MTI have been identified as a major concern, affecting the coupling between the Dirac states and the magnetic dopants. Nevertheless, details on the local magnetic order in these materials are not well understood. Here, we report the study of the magnetic correlations in thin films using a combination of muon spin relaxation (μSR), and magnetic soft x-ray spectroscopy and imaging. μSR provides two key quantities for understanding the microscopic magnetic behavior: The magnetic volume fraction, i.e., the percentage of the material that is ferromagnetically ordered, and the relaxation rate, which is sensitive to the magnetic static (≈μs) and dynamic disorder. By choosing different implantation depths for the muons, one can further discriminate between near-surface and bulk properties. No evidence for a surface enhancement of the magnetic ordering is observed, but, instead, we find evidence of small magnetically ordered clusters in a paramagnetic background, which are coupled. The significant magnetic field shift that is present in all samples indicates a percolation transition that proceeds through the formation and growth of magnetically ordered spin clusters. We further find that fluctuations are present even at low temperatures, and that there appears to be a transition between superparamagnetism and superferromagnetism.

DOI: 10.1103/PhysRevB.106.224425

I. INTRODUCTION

Topological insulators (TIs) have gained strong interest from the scientific community as a new class of materials with fascinating yet exotic physics which offers a large potential for applications in the field of spintronics [1–6]. TIs host a gapless topological surface state which exhibits a Dirac-cone-like dispersion. The topological surface state is protected by time-reversal symmetry (TRS) which leads to a variety of interesting effects. The prediction of novel quantized states arising from the peculiar coupling between magnetic and electric fields make TIs a perfect host for the next generation of electronic and spintronic devices. Materials of the Bi_2Se_3 family are among the simplest three-dimensional (3D) TIs. They exhibit a single Dirac cone at the Γ point and show a large bulk band gap [7], which makes them potentially well suited for room-temperature spintronics applications. The existence of the topological surface state has been confirmed by angle-resolved photoemission spectroscopy (ARPES) [8], scanning tunneling spectroscopy [9], and magnetotransport measurements [10]. Breaking the TRS of TIs, e.g., via magnetic doping with Mn [11], Cr, or V [12–16], is however a prerequisite for observing the quantum anomalous Hall effect (QAHE) [17–19], image magnetic monopoles [20], the giant magneto-optical effects [21], and the topological magnetoelectric effect. Potential applications of ferromagnetic TIs include memory cells and magnetic sensors [22], as well as novel electronic devices due to their tunable electronic properties [23].

The QAHE has been observed in Cr- and V-doped $(Bi,Sb)_2Te_3$ [24–28], completing the quantum Hall effect trio [24]. Thin films of undoped and doped Sb_2Te_3 have been prepared on a number of substrates, such as Si(111) [29], *c*-plane sapphire [30,31], and GaAs(100) [32], in part in the context of thermoelectrics research [33,34]. The topological surface

*steinkenj@ill.fr
†Present address: School of Physical Science and Technology, ShanghaiTech Laboratory for Topological Physics, ShanghaiTech University, Shanghai 200031, China.
‡Present address: Max Planck Institute of Microstructure Physics, Weinberg 2, 06120 Halle, Germany.
§thorsten.hesjedal@physics.ox.ac.uk

state in Sb_2Te_3 bulk crystals as well as molecular beam epitaxy (MBE) grown thin films [29] has been predicted [7] and experimentally confirmed by ARPES [35]. Upon doping with Cr [13] or V [36], these magnetic TI (MTI) materials show long-range ferromagnetic order with a magnetic transition temperature that is dependent on the doping concentration. In bulk crystals, where the solubility is low, T_C is 17 K [12] and 22 K [14] for Cr and V doping, respectively. As MBE is a low energy deposition technique, much higher doping concentration can be achieved in thin films, leading to very high T_Cs for Cr and V of 190 K [13] and 177 K [36], respectively. Further, doping with rare earth elements induces higher magnetic moment ions to the TI, which is, in principle, a route to increase the size of the magnetic gap [37,38]. Using MBE, heterostructures further offer the opportunity to design and control the magnetic behavior of a TI system by combining the desirable properties of their constituent layers [39–41]. A review of magnetic doping of the $(Sb,Bi)_2(Se,Te)_3$ 3D TI family can be found in Ref. [42].

Probing the domain structure and determining the magnetic anisotropy is particularly relevant for understanding the microscopic transport studies, and for future electronic device applications. First, in the QAH state, the existence of magnetic domains fully controls the transport properties. Whereas single-domain systems host a single chiral edge channel with a quantized Hall resistivity of h/e^2, multidomain systems exhibit chiral edge channels also at the magnetic domain walls [6]. These domain-wall bound chiral edge channels were directly observed using scanning probe microscopy techniques [43–45]. Second, the uneven spatial distribution of magnetic dopants can lead to a spatial variation of the magnetic gap—a phenomenon known as Dirac-mass disorder—which was directly imaged on the atomic scale using spectroscopic imaging scanning tunneling microscopy [46].

Most commonly, magnetic domains and domain walls in thin films and bulk crystals are imaged using, e.g., magnetic force microscopy (MFM), magneto-optic Kerr microscopy, or x-ray magnetic circular dichroism (XMCD) based photoemission electron microscopy (XPEEM). Each of the methods has its unique advantages and limitations, e.g., in terms of lateral resolution, magnetic sensitivity, and temperature and applied magnetic field limitations. Using field- and temperature dependent MFM, bubblelike ferromagnetic domains measuring ≈500 nm were observed in thin films of the Cr-doped magnetic TI $(Bi_{0.1}Sb_{0.9})_2Te_3$ [47], and also V-doped Sb_2Te_3 [48]. However, as magnetic TI thin films are usually magnetically very soft, the magnetic stray field of the MFM tip can be detrimental for the precise determination of magnetic domains.

Here, we present a study of magnetic inhomogeneities of Cr-doped Sb_2Te_3 films on *c*-plane sapphire using XMCD and XPEEM and muon spin rotation. Films with a doping concentration of up to $x = 0.76$ in $Cr_xSb_{2-x}Te_3$ have been prepared, which were ferromagnetic [49], of high structural quality, and free of secondary phases and precipitates, consistent with previous reports by Gupta *et al.* [50] of an upper bound of $x = 0.88$ for the absence of phase separation and precipitates. The choice of the upper doping limit was motivated by the onset of changes in the magnetic properties, rather than by the deterioration of the structural properties (high quality films with $x = 0.88$ have been reported by Gupta *et al.* with a T_C of 250 K). The magnetic transition temperature is an almost linear function of doping concentration, reaching up to a maximum of 168 K for $x = 0.71$ in our samples. This value is slightly lower than the value of 190 K reported by Zhou *et al.* [13] for $x = 0.59$.

II. EXPERIMENTAL METHODS

A. Sample preparation and characterization

$Cr_xSb_{2-x}Te_3$ thin film samples were prepared by MBE on *c*-plane sapphire substrates in a doping range from $x = 0.15$ to 0.71, as discussed in detail for $x \leqslant 0.42$ in Ref. [51]. In short, we employed a two-step deposition method, where an undoped nucleation layer is first deposited at a lower substrate temperature, followed by the growth of the doped $Cr_xSb_{2-x}Te_3$ film at a higher substrate temperature. Standard effusion cells were used, whereby a Te:(Cr + Sb) overpressure of 10:1 was kept. The growth rate was ≈0.6 nm/min and a series of samples were grown with varying Cr doping concentrations and a thickness of ≈55 nm.

The structural properties of the films were monitored *in situ* using reflection high energy electron diffraction (RHEED), showing streaky RHEED patterns which are indicative of smooth two-dimensional growth [51]. *Ex situ* characterization was done by atomic force microscopy for the surface morphology, and the crystalline properties and the film thickness were determined by x-ray diffraction and reflectivity (XRR) [51], to determine the maximum Cr concentration up to which the films remain of high quality and free from secondary phases [51]. Rutherford back-scattering spectrometry (RBS) was used for accurate determination of film thickness and Cr concentration [51].

The (integrated) magnetic response of the thin films was determined using a superconducting quantum interference device (SQUID) vibrating sample magnetometer (VSM). The Quantum Design MPMS 3 SQUID-VSM system allows for the application of magnetic fields of up to 7 T and measurement temperatures of below 2 K. Hysteresis loops of the magnetization M were measured at selected temperatures with the magnetic field H applied both in plane and out of plane. The hysteresis loops for a sample with $x = 0.71$ (in $Cr_{0.71}Sb_{1.29}Te_3$) at 5 K [Fig. 1(a)] reveal their perpendicular magnetic anisotropy (easy axis parallel to the surface normal *c* axis) and a saturation magnetization of ≈2.9 μ_B/Cr, consistent with the previously reported, *x*-independent value for the series of (2.8 ± 0.2) μ_B/Cr. The magnetic moment per Cr ion was obtained by determining the film volume (using the XRR thickness) and the doping concentration as determined by RBS for the sample series. The saturation value is close to the Hund's rules value 3 μ_B/Cr, whereby the slightly reduced value is to be expected due to the hybridization between Cr-*d* and Se-*p* orbitals [51,52].

The magnetic transitions, and associated transition temperatures T_C, were obtained by recording $M(T)$ plots (in an applied out-of-plane field of 20 mT), as shown for the $x = 0.71$ sample in Fig. 1(b) (red curve). The $M(T)$ plots were differentiated with respect to temperature, where the minima are taken as the value of T_C. The films with $x \leqslant 0.41$ show a single, strongly doping concentration dependent transition

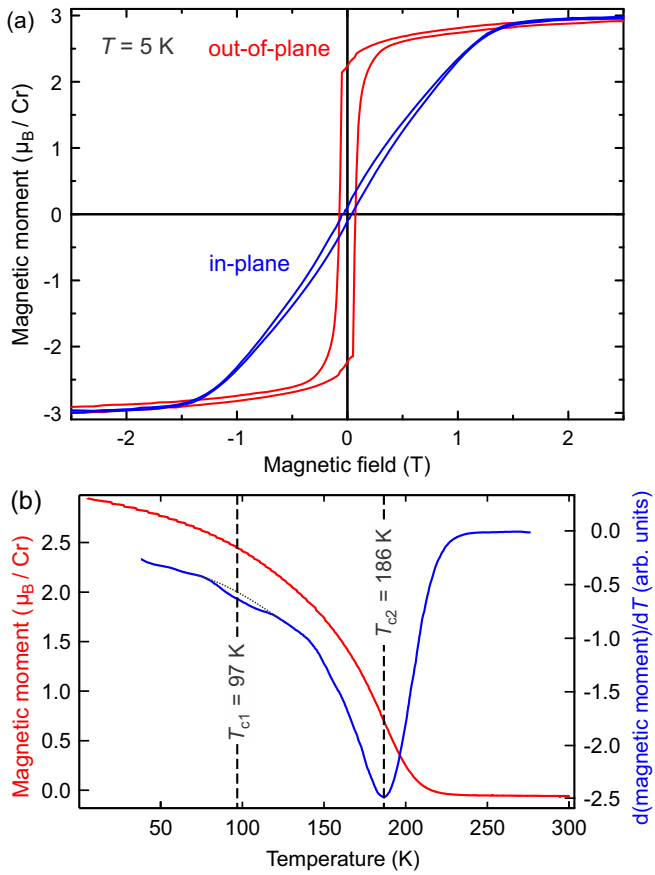

FIG. 1. (a) $M(H)$ hysteresis loops for a $Cr_{0.71}Sb_{1.29}Te_3$ thin film sample with the field applied in plane (blue) and out of plane (red). The data were taken at 5 K. (b) The temperature dependent magnetization, $M(T)$, was measured in an applied out-of-plane field of 20 mT during cooldown (red curve). The differentiated curve (shown in blue) reveals two transition temperatures.

temperature, ranging from 28 K for $x = 0.15$, over 65 K for $x = 0.26$, to 125 K for $x = 0.42$ [51]. In case of the highly doped sample, two transitions are found, as shown in Fig. 1(b) (blue curve). Apart from the transition at 186 K, which is consistent with the behavior of the doping series, a second, much weaker and less obvious transition appears at ≈97 K. Note that this sample shows no hints of secondary phases either, yet was deemed to be the limit for the Cr doping series due to the magnetic anomaly.

An overview of the structural and magnetic properties for the $Cr_xSb_{2-x}Te_3$ sample series is given in Ref. [51], and their magnetotransport properties are discussed in Refs. [49,53]. In summary, the *p*-type samples had carrier concentration ranging from 5.83 to 11.52 × 10^{13} cm^{-2} and mobility ranging from 207 to 28 cm^2/Vs for $x = 0.15$–0.76, respectively, as determined by transport measurements [49]. The observed $T_C \sim xp^{1/3}$ relationship is in agreement with previous studies on these materials [13,54], and consistent with the proposed Ruderman-Kittel-Kasuya-Yoshida interaction within the mean-field approximation [55].

B. X-ray magnetic circular dichroism

X-ray absorption spectroscopy (XAS) and XMCD [56–58] experiments were performed at the Cr $L_{2,3}$ edges on beamline I10 at the Diamond Light Source, UK. Measurements were performed after *in situ* cleaving in the UHV environment of the intermediate chamber of the superconducting magnet end station. The XMCD was obtained as the difference $(\mu^- - \mu^+)$ between two XAS spectra recorded with the helicity vector antiparallel and parallel to the applied magnetic field of 2 T, where μ^+ and μ^- are the absorption coefficients for parallel and antiparallel alignment of x-ray helicity vector and magnetization direction, respectively. Measurements were performed by reversing the polarization of the normal incidence x rays, to avoid having to switch the high field of the superconducting magnet, at normal incidence with respect to the sample surface, using total-electron-yield detection mode [58].

C. X-ray Photoemission Electron Microscopy

XPEEM [59] was carried out on the XPEEM beamline (UE49-PGM) at the BESSY II synchrotron in Berlin [60]. In essence, XPEEM is an XMCD-based electron microscopy (with the photon energy in our case tuned to the Cr L_3 edge), which spatially resolves the emitted photoelectrons. The XPEEM image contrast is directly proportional to the relative orientation of the x-ray helicity $\hat{\mathbf{P}}$ and the magnetization direction $\hat{\mathbf{M}}$, i.e., ranging from bright contrast ($\hat{\mathbf{P}} \uparrow\uparrow \hat{\mathbf{M}}$), over gray (no contrast for $\hat{\mathbf{P}} \perp \hat{\mathbf{M}}$), to dark contrast ($\hat{\mathbf{P}} \uparrow\downarrow \hat{\mathbf{M}}$) [57,61]. XPEEM provides the spatially resolved magnetization of a sample surface with a resolution down to ≈40 nm over a 5-μm field of view. The sample holder allows for low temperature measurements down to ≈45 K, in a constant applied field of up to 22 mT (or a briefly applied field of up to 50 mT) [60]. Prior to XPEEM imaging, the thin film samples were sputter cleaned at a pressure of 1.2 × 10^{-5} mbar, using a current of $I = 20$ μA for 10 min each at energies of 1.1 keV, 800 eV, and finally 400 eV. This sequence yields a clean TI surface [62], free of oxidation [63], and of higher quality compared to the surface after decapping of Se or Te [64].

D. Low energy muon spin relaxation

Weak transverse field (wTF) and zero-field (ZF) muon spin relaxation (μSR) measurements were carried out at the low energy muon (LEM) beamline at the Paul Scherrer Institut, Switzerland [65]. The data were collected as a function of implantation energy and temperature. The LEM beamline produces a spin polarized beam of very slow muons within a tunable energy range of 1–30 keV, through which the muon implantation depth can be tuned. Muon stopping distributions were estimated by carrying out Monte Carlo simulations using the Trim.SP software [66]. The samples were glued onto Ni-coated sample holders. All muons stopping in the sample holder depolarize very quickly, within the first 100 ns, and do therefore not contribute to the overall relaxation rate beyond this time interval. One sample was glued to an Ag coated sample holder, which gives only a time independent background signal, to allow for the study of fast relaxation components in zero-field measurements. In a μSR experiment, the spins

of the implanted muons experience a combination of external and local, internal magnetic fields, and they will precess around the net field. A muon will eventually decay, with a mean lifetime of 2.2 µs, emitting a positron preferentially along the direction of the muon spin at the time of decay. By following the time evolution of the polarization of the muon ensemble detailed information of the local magnetic field distribution within the sample can be obtained.

In wTF measurements, a field perpendicular to the μ spin is applied. In the absence of any other magnetic fields the μ spin will precess around the external field with the characteristic Larmor frequency of $\omega = \gamma_\mu B_{\text{ext}}$, with the muon gyromagnetic ratio of $\gamma_\mu = 2\pi \times 135.5$ MHz/T. If static magnetic order develops the internal fields will be comparatively strong and if there is a distribution of fields at the muon stopping site(s) a fast relaxation will be observed. In contrast, if the muon stops in a paramagnetic environment, the muon mainly experiences the external magnetic field, and only a very slow relaxation is observed. By following the fraction of the muon population that undergoes slow precession the nonmagnetic volume fraction of the sample can be estimated. The data were fitted using the following equation:

$$A(t) = ae^{-\lambda t}\cos(\omega t + \phi)\ . \tag{1}$$

Here, $A(t)$ is the time dependent asymmetry between the positrons detected on opposing sides of the sample, a is the oscillation amplitude at $t = 0$ which is proportional to the nonmagnetic volume fraction, λ is a relaxation parameter linked to static and dynamic field distribution in the system, ω is the μ-precession frequency which is proportional to the average magnetic field experienced by the muon via the gyromagnetic ratio as explained above, and ϕ is a phase which depends on the orientation of the initial polarization relative to the sample-positron detector axis and is in general fixed for a given instrumental setting. The total nonmagnetic volume fraction can be estimated by comparing the remaining asymmetry amplitude to that of the fully nonmagnetic state after correcting for unwanted contributions from the instrument, sample holder, and exposed parts of the substrate (see, e.g., Refs. [67,68]). For our samples these parasitic contributions amounted to 6% of the observed signal.

III. RESULTS

Combining magnetic spectroscopy and imaging with the local and dynamic sensitivity of muons, we studied the Cr doping series. We focus on $Cr_xSb_{2-x}Te_3$ films with $x \leqslant 0.42$, i.e., films which show no secondary phases and are characterized by sharp RHEED streaks and only weakly broadened x-ray reflections. However, as XPEEM does not show any magnetic contrast for films with $x \leqslant 0.42$, owing to its relatively high base temperature and potentially limited by its lateral resolution (of ≈40 nm), this part of the paper focuses on $x = 0.71$ samples.

A. Magnetic x-ray spectroscopy

Figure 2 shows the Cr $L_{2,3}$ XAS and XMCD spectra of the $Cr_{0.71}Sb_{1.29}Te_3$ thin film sample, obtained after *in situ* cleaving. The XAS line shape is clean and shows no

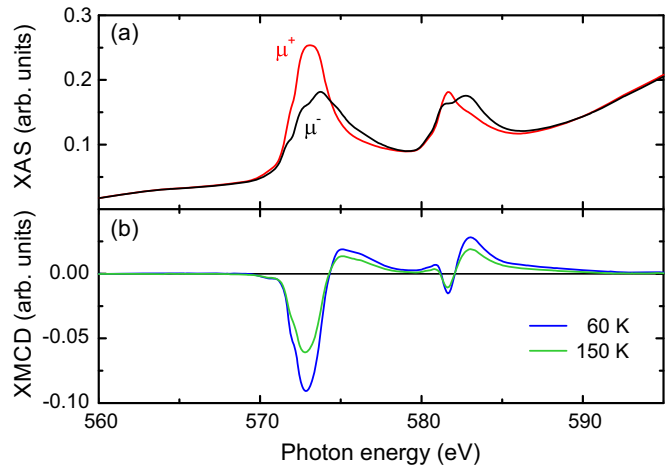

FIG. 2. Cr $L_{2,3}$ spectra of Cr-doped Sb_2Te_3 ($x = 0.71$) in an applied out-of-plane field of 2 T. (a) XAS spectra for opposite circular polarizations (μ^-, μ^+) in normal incidence at 60 K. (b) XMCD ($\mu^- - \mu^+$) spectra at 60 K (blue line) and 150 K (green line).

evidence of oxidation [52,69]. It is further suggesting a nominal Cr valence of 2+, indicative of substitutional Cr doping (on Bi/Sb sites). The XAS and XMCD spectra are similar to previously reported measurements on bulk Cr-doped $(Sb,Bi)_2Te_3$ [39,70]. The decrease in amplitude of the XMCD signal at 150 K compared to that at 60 K reflects the magnetization reduction as the temperature increases; however, no fundamental difference in line shape is observed in the spectra at the two temperatures.

For the XPEEM measurements, the samples were not cleaved *in situ*, but sputter cleaned. The cleaning process was optimized such that it yielded an identical XAS spectrum, free of signs of oxidation, to the *in situ* cleaved samples. Figure 3 shows an XPEEM image of a $Cr_xSb_{2-x}Te_3$ film with $x = 0.71$ at 54.7 K, i.e., below both transition temperatures of $T_{c1} = 97$ K and $T_{c2} = 186$ K found in bulk-sensitive SQUID magnetometry (see Fig. 1). The contrast reveals strongly inhomogeneous magnetic order down to length scales below 100 nm.

Next, we investigated the temperature dependence of the magnetic domain pattern, to shed some light on the two magnetic transitions. Figure 4 shows a series of XPEEM images, obtained at temperatures ranging from 46.5 K (the base temperature of the cryostat in combination with the chosen sample holder) to 100.8 K, which is above T_{c1}. Whereas the contrast shows little variation up to 90.7 K, i.e., no change in the distribution of magnetic domains, the image taken at 100.8 K shows almost no contrast at all. Note that the black and white pattern in the center of the image is due to a magnetic defect, which was also used for optimizing the focus. The absence of any measurable contrast above T_{c1}, together with the clearly existing ferromagnetic long-range order that is evident in the SQUID data [Fig. 1(b)] and the XMCD [Fig. 2(b)] taken at 150 K, suggests that the lower transition temperature represents a blocking temperature. It is very unlikely that the magnetic state between T_{c1} and T_{c2} is due to a secondary phase, which should also be structurally distinguishable. One of the most likely secondary phase candidates, Cr_2Te_3, has

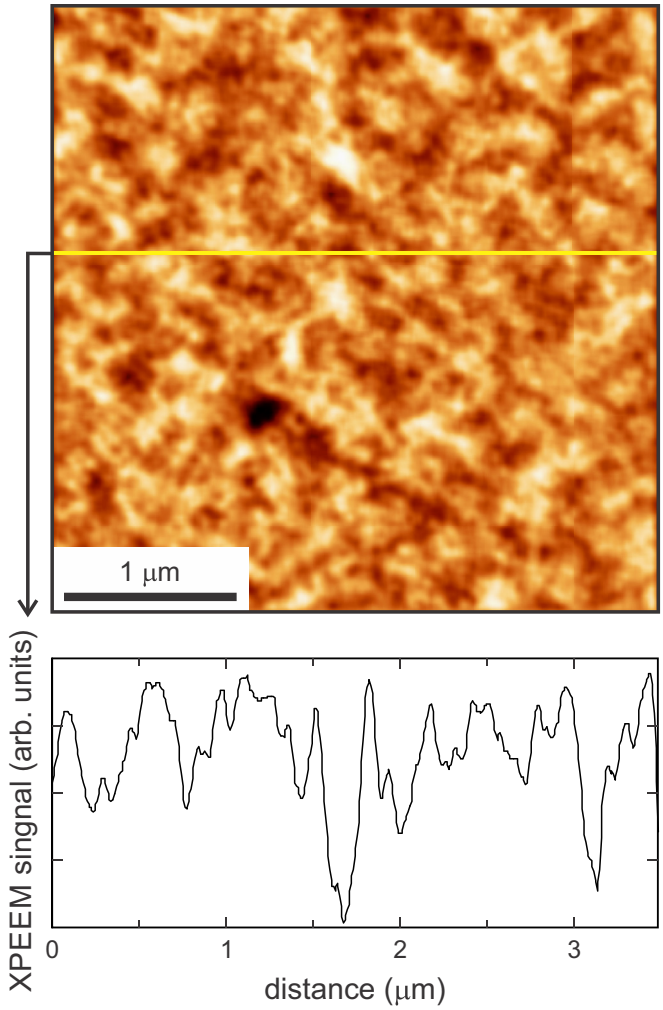

FIG. 3. XPEEM image taken of the magnetic domain structure of a Cr-doped Sb_2Te_3 with $x = 0.71$ taken at 54.7 K and the x-ray energy of the Cr L_3 edge. The lower panel shows a linescan of the XPEEM contrast at the indicated position in the image. The XPEEM contrast has been normalized.

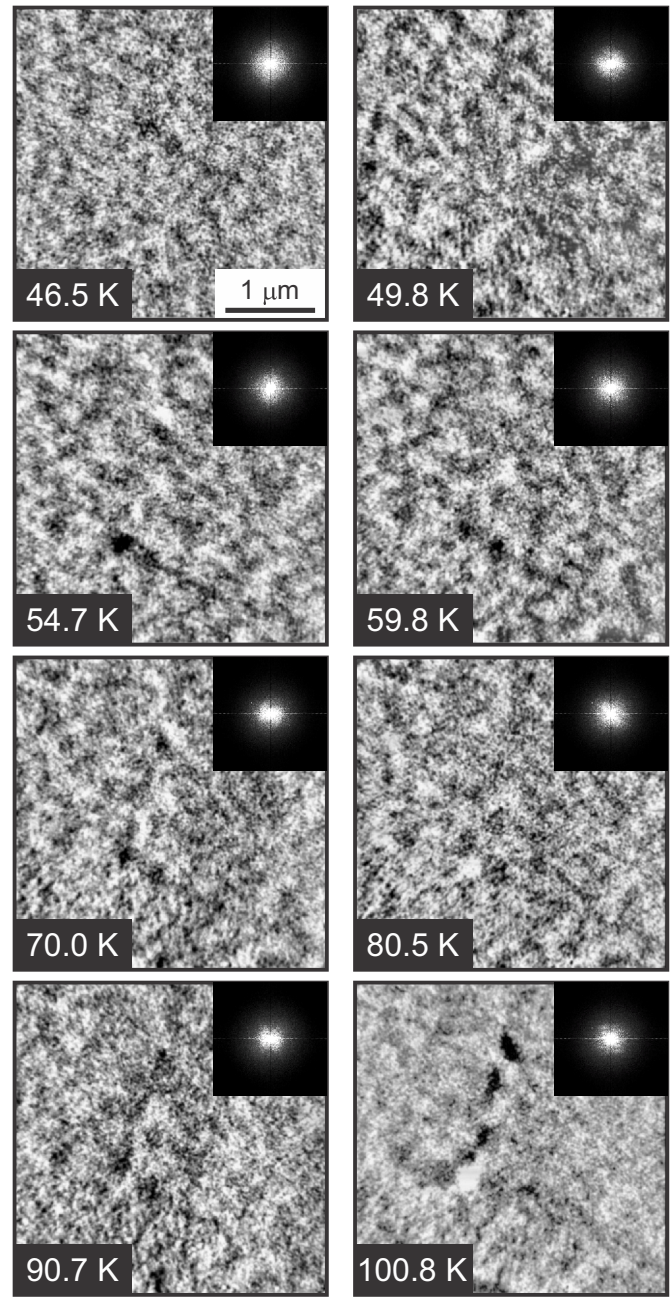

FIG. 4. XPEEM images, taken at the Cr L_3 edge at different temperatures ranging from 46.5 to 100.8 K. The scale bar (1 μm) is shown in the top-left image, and is the same for all temperatures. In the top-right corner of each image, a Fourier transform of the contrast is shown. The XPEEM contrast has been normalized.

a T_C of 150 K and can be ruled out as the XMCD persist above 150 K [Fig. 2(b)]. Further, the spectral shape of the measured XMCD differs from the one measured on Cr_2Te_3 thin films [71]. Note that there are other possible secondary phase candidates as well, such as trigonal $Cr_{0.6}Te$, monoclinic Cr_3Te_4, and cubic Cr_5Te_8 [72], which have reported T_C values of 238, ≈330, and 250 K, respectively [73]; however, none of them has been structurally identified in our films.

Overall, the occurrence of two magnetic transitions in these thin films, with no evidence for the presence of secondary phases, hints at T_{c1} being a blocking temperature below which superparamagnetic domains freeze-out. To further clarify this behavior, to discriminate between bulk and surface magnetism in the films, and to study the timescales of the fluctuations, we carried out complementary μSR measurements.

B. Muon spin relaxation

μSR spectra were acquired at two implantation depths, with the energy of the muons chosen to be 3 and 6 keV (5 keV for the slightly thinner $x = 0.05$ sample). The stopping profile distributions are shown in Fig. 8 in the Appendix for those energies. The lower energy places the center of the distribution near the surface of our films, whereas the higher energy places it near the middle layer of the film.

Figures 5(a), 5(b), and 5(c) show the extracted fit parameters, the magnetic volume fraction, slow relaxation rate, and internal magnetic field, as a function of temperature for all concentrations and the two implantation depths. The magnetic transition is concentration dependent and can be clearly

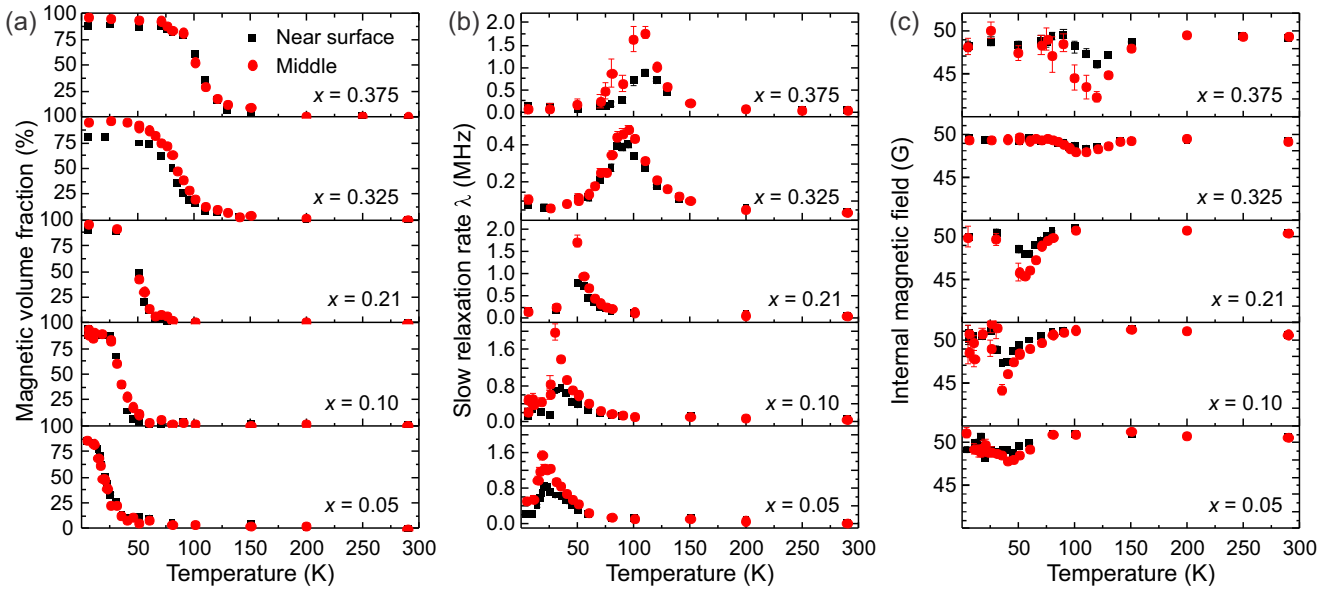

FIG. 5. (a) Magnetic volume fraction, (b) muon slow relaxation rate, and (c) internal magnetic field as a function of temperature and depth for the five Cr concentrations as extracted from the wTF measurements under an applied field of 50 G. The data from the near surface area are shown by black squares and the data from the middle of the film are shown by red circles.

identified for all samples. The slow relaxation rate peaks around the magnetic transition, but this peak is very broad, and for the two lower Cr concentrations ($x = 0.05$ and 0.1) the relaxation rate does not fully decay in the magnetically ordered phase. The magnetic transition is also clearly visible as a step in the magnetic volume fraction, where some magnetic features seem to persist into the nonmagnetic phase.

The magnetic volume fraction is >90% for all Cr concentrations above 0.05, and close to 95% in the middle of the films. The volume fraction near the surface is generally very similar to the center, i.e., no surface enhancement was found, though there might be a small reduction at the film surface for the higher concentrations. For the lowest concentration, the total magnetic volume fraction reaches 85% both in the middle and near the surface of the film. Figure 6 shows a comparison of the Cr concentration dependence of the magnetic volume fraction at 4 K.

The Curie temperature, as measured by the peak in the relaxation rate, is also identical for the middle and the surface regions in these samples. As expected, this temperature is also in good agreement with the temperature at which half of the total magnetic volume has developed. The relaxation rate—a measure of the field distribution at the muon stopping site—shows a very broad peak around the magnetic transition temperature. For the higher doping concentrations, the relaxation rate is suppressed at the lowest temperatures deep in the ordered phase but for lower concentrations significant fluctuations remain even at the lowest temperatures accessible. In contrast to the transition temperature and magnetic volume, the value of the relaxation rate is significantly reduced near the film surface when compared to the bulk.

All samples show strong internal magnetic field shifts as they proceed through the transition. These tend to recover as the sample enters the magnetically ordered phase—except for the lowest doping concentration under investigation. For this sample, a small reduction in the internal magnetic field persists down to low temperatures. Like the magnetic relaxation amplitude, the amplitude of the field shift is reduced near the surface of the samples even though the temperature dependence remains the same.

wTF measurements were also carried out on the $x = 0.1$ sample after zero-field cooling (not shown), and we found that the internal field shift is much less pronounced near the middle of the film. Further, there is also a less pronounced reduction in the shift near the surface.

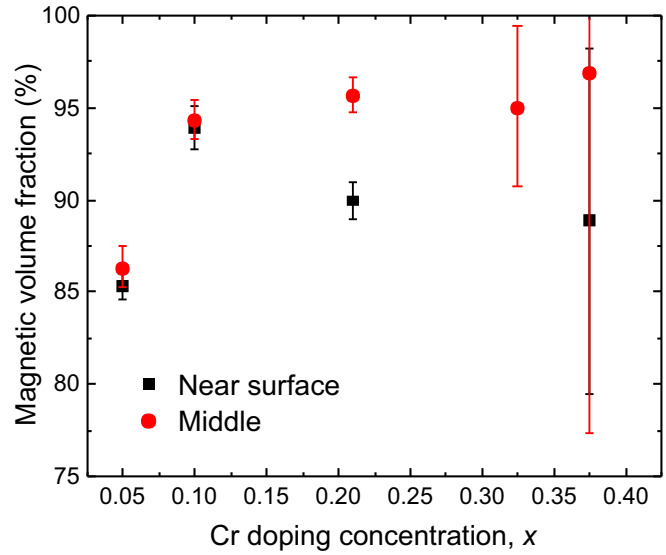

FIG. 6. Magnetic volume fraction as a function of Cr doping concentration at 4 K, both near the surface and in the middle of the films.

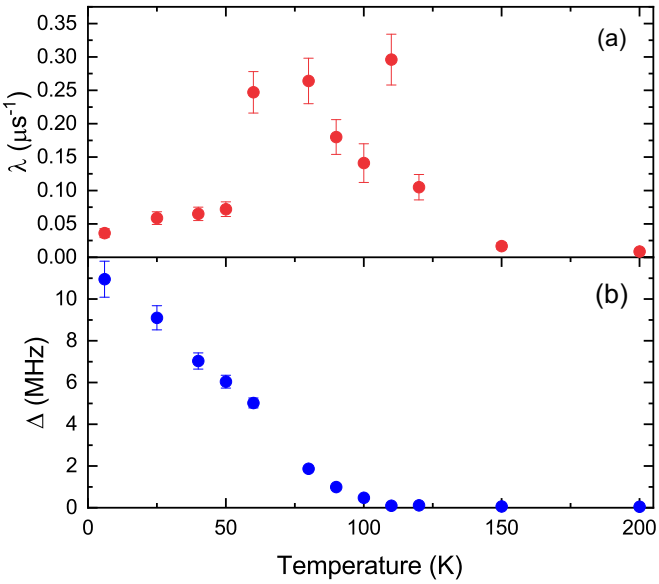

FIG. 7. Zero-field measurement of the $x = 0.325$ sample at 6 keV, and fit parameters vs temperature: (a) slow relaxation component λ and (b) fast relaxation component Δ.

Additional zero-field measurements were carried out on the $x = 0.325$ sample at 6 keV to investigate the magnetically ordered phase further. In this configuration, a precession signal would reveal a highly ordered ferromagnet, provided the number of possible muon stopping sites is small, and a fast exponential relaxation is then indicative of a disordered magnet. Above the transition our data follow a single exponential decay, while below the transition the data are well described by a fast and a slow relaxing component using the following equation: $A(t) = A_0[\frac{1}{3}\exp(-\lambda t) + \frac{2}{3}\exp(-\Delta t)] + A_{bg}$ (see Fig. 7). Below the transition λ is indicative of the amount of dynamic fluctuations in the system: This term in the equation represents the ensemble average of muons that are implanted with their spins parallel to the local magnetic field which can only relax due to dynamic fluctuations of the local field. In line with the wTF measurements we find a broad peak around the magnetic transition that decays slowly in the ordered regime. The fast relaxation rate is determined by the width of the static field distribution at the muon stopping sites. It continues to increase monotonically in the ordered regime down to the lowest temperatures. The maximum width obtained at 6 K was 0.013 T.

IV. DISCUSSION

One question that affects the interplay of magnetism and transport behavior in these compounds is the homogeneity of the magnetic properties. Hereby, one can distinguish between (i) surface-versus-bulk effects, possibly hinting at an enhancement of the magnetic order involving the topological surface state, and (ii) the homogeneity throughout the volume of the sample. There have been contradicting reports on surface magnetism in the literature, either reporting different magnetic anisotropy and transition temperatures at the surface [55,74], or finding no evidence for it at all [39,70]. In the latter studies, surface-sensitive XMCD was employed which is able to assure an unoxidized surface. Given that these compounds are prone to oxidation [63], and slight changes in stoichiometry are possible due to the desorption of a protective cap [64], differences between surface and bulk properties are not too astonishing. Our μSR results indicate that there is no significant difference in either the magnetic volume fraction or transition temperature between surface and bulk for all doping concentrations that were investigated.

The very broad peak in the slow relaxation rate indicates a transition characterized by the random distribution of dopants; some magnetic fluctuations and residual magnetic correlations are present above the transition temperature gradually increasing as the temperature decreases across the magnetic transition. The character of the transition does not markedly change with decreasing doping concentration, though for lower concentrations some fluctuations can still be detected even at the lowest temperatures. For the lowest concentration under investigation, the total magnetic volume fraction is also reduced.

Despite the significant amount of randomness characterized by the μSR data, all films clearly undergo a magnetic phase transition and enter a magnetically ordered phase at low temperatures. This is in line with studies of V-doped magnetic TIs [68], and in contrast to Dy-doped TIs where no clear transition was found, but, instead, a gradual increase of short-range (patchy) magnetic order [38].

The shift in the magnetic field experienced by the muons can be explained by the formation of small magnetically ordered clusters, i.e., the presence of magnetic inhomogeneities in the sample. Muons stopping within these clusters will depolarize quickly and not contribute to the slow precession signal in wTF measurements. Muons stopping in the paramagnetic regions surrounding the clusters will experience a distribution of magnetic stray fields emanating from the surrounding clusters that are preferentially aligned along the external magnetic field direction, parallel to the c axis of the crystal. The effective field experienced by these muons will depend on the number of surrounding clusters and their distribution, the strength of the intracluster coupling, and the frequency of the magnetic fluctuations. If the clusters are relatively small, rather than columnar domains traversing the entire film thickness, the muons stopping in the middle of the film will be surrounded by magnetically ordered, fluctuating patches, whereas muons stopping near the surface experience no stray fields from above their stopping site. This explains why the field shift is smaller near the surface compared to the middle of the film even though the magnetic volume fraction remains constant. In the magnetically ordered phase, the magnetic volume fraction is close to 100%, thus very few muons will stop in the paramagnetic region of the film and the internal field measured is dominated by muons stopping outside the sample. Additional measurements after zero-field cooling support this picture. The size of the field shift is significantly reduced as the effective stray fields from randomly aligned clusters tend to partially cancel each other; in practice, the clusters are very likely still aligned with the easy c axis in the material, but with no preferential direction. The reduction in field shift is significantly more pronounced for muons stopping in the middle of the film. This supports the idea that these muons are surrounded by, and experience the influence of, many

clusters, which are therefore relatively small, i.e., significantly smaller than the film thickness. In contrast, muons stopping near the surface have only few clusters contributing to their stray field environment. Hints of the cluster formation can also be seen in the XPEEM measurements (of the highly doped sample).

In the ZF measurements, we find a continued increase of the fast relaxation constant Δ even in the magnetically ordered regime. The effective field distribution which the muons experience in the ordered phase continues to increase even when the magnetic volume fraction is close to 100%. This implies that the percolated, magnetically ordered patches continue to be only weakly coupled, with superparamagnetic fluctuations persisting at low temperatures. The muon spins are exposed to the fluctuating stray fields of the neighboring patches, reducing the effective field they are subjected to. As these thermal fluctuations slow with decreasing temperature and clusters might freeze or get pinned, the effective static field distribution increases.

Using scanning SQUID-on-tip microscopy, Lachman *et al.* [75] first observed that the magnetic domains in weakly Cr-doped $(Sb,Bi)_2Te_3$ continue to fluctuate even below liquid He temperatures. Their measurements showed that the magnetic order in these films is not robust over long length scales. In the most strongly doped sample of our series, which was investigated only with XPEEM, we find evidence for a blocking temperature, most likely from superparamagnetism to superferromagnetism, well below T_C. Below this temperature, the magnetic order is frozen and thus XPEEM imaging was able to directly observe the strong inhomogeneities in the magnetization distribution.

The nature of the magnetic order in Cr- and also V-doped TIs has been studied using a variety of techniques [15,51,76,77]. The key finding was that the ferromagnetic transition temperature is doping concentration dependent, contradicting earlier theoretical explanations by the Van Vleck model [78] which rely on intra-atomic interactions as these only give a concentration independent contribution [19,24,79]. Instead, the covalent character of magnetically doped compounds in this class of materials is the crucial ingredient [77]. Despite finding an impurity band near the Fermi level [67,80,81], the hybridization between the dopant $3d$ and the $5p$ states of the host material [39,70,77,80,82] appears the most important mechanism stabilizing ferromagnetism.

Recent theoretical advances have also critically revisited the Van Vleck model of the magnetic order and made the link to other dilute magnetic semiconductors, pointing instead to dominant superexchange interaction in II-VI compounds and the transition metal doped tetradymite dichalcogenides independent of their topological state [83]. For Cr- and V-doped TIs a ferromagnetic exchange based on the charge state of the magnetic impurity is predicted [83].

Further, the ferromagnetic order in these compounds can be efficiently controlled via the electrical carrier concentration, either through charge doping whereby T_C increases with the carrier concentration [70,82], or through electrical gating [75]. Putting these pieces together, it can be stated that magnetic order in these TI compounds is strongly dependent on a carrier-mediated interaction based on hybridized dopant $3d$ and host p states, forming carrier bands, with some analogies to the ordering mechanism in dilute magnetic semiconductors [84,85].

In agreement with V doping [67,68], we find that for lower doping concentrations a significant fraction of the material remains paramagnetic. The fact that neither the volume fraction nor the transition temperature changes significantly between surface and film center suggests a long-range magnetic ordering mechanism that does not depend strongly on very short-ranged interactions. In addition, our doping concentrations are much below the site percolation thresholds for triangular or honeycomb lattices (see Ref. [67]).

In other dilute magnetic semiconductors the magnetic ordering mechanisms have been extensively investigated. There, it was found that percolation dynamics of bound magnetic polarons should dominate if the localization length of the hole carriers is short compared to the mean impurity distance. This distance spans ranges from approximately 200 to 20 Å in our samples, depending on the impurity concentration, assuming homogeneously distributed impurities. It was pointed out in Ref. [86] that the percolation behavior is a very general phenomenon, and does not depend on the details of the material investigated (mostly GaMnAs in their case). From our muon results, it can be concluded that this model is also applicable for Cr-doped Sb_2Te_3 for all doping concentrations investigated. In Ref. [85], μSR revealed a phase separation into FM and PM regions in the dilute magnetic semiconductor GaMnAs, persisting down to the lowest temperatures accessible, but no magnetic clustering or percolation was found there, leading to the conclusion that the hole localization length is much greater than the mean impurity distance in those samples. Our samples do show a percolation transition and magnetic clustering, as evidenced by the internal magnetic field shifts. In addition the continuing increase in the static field distribution in the magnetically ordered phase lends additional support to the idea of percolating magnetically ordered patches, and this is also in contrast to the observations on GaMnAs where no change in the magnetic field distribution was seen below the ordering temperature [85]. This clearly points to more localized carriers in Cr-doped Sb_2Te_3 with localization lengths that appear to be comparable to the mean impurity distance. The magnetic ordering mechanisms in these samples are clearly very complex and our data show that they display characteristics of magnetic ordering of both localized and itinerant carriers at the same time.

V. SUMMARY AND CONCLUSIONS

In conclusion, we presented an investigation of the magnetic order in MTIs, with a focus on the homogeneity of the magnetic sample properties, which is relevant for studying effects based on QAH states.

Using μSR, we find that there is no significant difference between surface and bulk magnetism for all doping concentrations studied. Moreover, we found that for low-doped films, which are the most relevant for QAH-based studies, a significant fraction of the film remains paramagnetic at low temperature. From the shift of the magnetic field experienced by the muons it can be concluded that small magnetic clusters are present in the sample, and that the coupling of these

clusters gives rise to apparent differences between the surface and the middle of the film. This observation addresses the other aspect of homogeneity with respect to magnetic order, i.e., its spatial distribution. From the observation of a percolation transition, it can be concluded that due to the random distribution of dopants the film is inhomogeneously magnetically ordered, an observation also supported by magnetic microscopy. The magnetic transition itself is dominated by carrier mediated interactions which remain nevertheless fairly localized, with localization lengths that appear to be comparable to the mean impurity distance, leading to a complex magnetic behavior. Being able to control these inhomogeneities will be the key to unlock the full potential of MTIs, which show nevertheless great potential for quantum device applications.

ACKNOWLEDGMENTS

This publication arises from research funded by the John Fell Oxford University Press Research Fund. Low energy μSR measurements were carried out at the LEM instrument at the Swiss Muon Source, Paul Scherrer Institut, Villingen, Switzerland. SPEEM measurements were carried out on beamline UE49 at the Helmholtz-Zentrum Berlin für Materialien und Energie, Germany. XAS and XMCD measurements were carried out on beamline I10 at the Diamond Light Source, UK, under Proposal No. SI-11503. The research leading to these results has received funding from the European Community's Seventh Framework Programme (FP7/2007-2013) under Grant No. 312284. J. Krieger gratefully acknowledges support by the Swiss National Science Foundation (Grant No. 200021_165910). We thank L. J. Collins-McIntyre for technical assistance with the sample growth, and A. A. Baker and P. Schönherr for help with the initial XPEEM experiments.

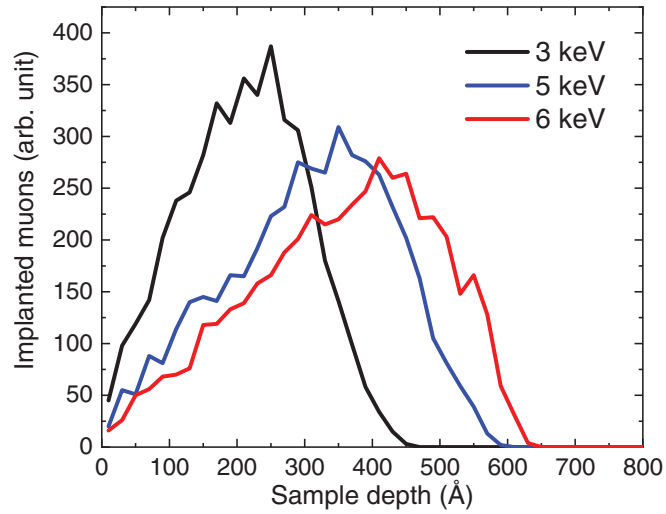

FIG. 8. Muon stopping profiles as a function of sample depth for the implantation energies used in this paper. A depth of 0 Å denotes the sample surface.

APPENDIX: IMPLANTATION ENERGY DEPENDENCE OF THE MUON STOPPING PROFILES

Figure 8 shows the muon stopping probabilities as a function of depth for the different implantation energies used in this paper.

[1] C. L. Kane and E. J. Mele, Z_2 Topological Order and the Quantum Spin Hall Effect, Phys. Rev. Lett. **95**, 146802 (2005).
[2] B. A. Bernevig, T. L. Hughes, and S.-C. Zhang, Quantum spin Hall effect and topological phase transition in HgTe quantum wells, Science **314**, 1757 (2006).
[3] L. Fu, C. L. Kane, and E. J. Mele, Topological Insulators in Three Dimensions, Phys. Rev. Lett. **98**, 106803 (2007).
[4] X.-L. Qi and S.-C. Zhang, The quantum spin Hall effect and topological insulators, Phys. Today **63**(1), 33 (2010).
[5] J. E. Moore, The birth of topological insulators, Nature (London) **464**, 194 (2010).
[6] M. Z. Hasan and C. L. Kane, *Colloquium*: Topological insulators, Rev. Mod. Phys. **82**, 3045 (2010).
[7] H. Zhang, C.-X. Liu, X.-L. Qi, X. Dai, Z. Fang, and S.-C. Zhang, Topological insulators in Bi_2Se_3, Bi_2Te_3 and Sb_2Te_3 with a single Dirac cone on the surface, Nat. Phys. **5**, 438 (2009).
[8] D. Hsieh, D. Qian, L. Wray, Y. Xia, Y. S. Hor, R. J. Cava, and M. Z. Hasan, A topological Dirac insulator in a quantum spin Hall phase, Nature (London) **452**, 970 (2008).
[9] P. Roushan, J. Seo, C. V. Parker, Y. S. Hor, D. Hsieh, D. Qian, A. Richardella, M. Z. Hasan, R. J. Cava, and A. Yazdani, Topological surface states protected from backscattering by chiral spin texture, Nature (London) **460**, 1106 (2009).
[10] D.-X. Qu, Y. S. Hor, J. Xiong, R. J. Cava, and N. P. Ong, Quantum oscillations and Hall anomaly of surface states in the topological insulator Bi_2Te_3, Science **329**, 821 (2010).
[11] Y. S. Hor, P. Roushan, H. Beidenkopf, J. Seo, D. Qu, J. G. Checkelsky, L. A. Wray, D. Hsieh, Y. Xia, S.-Y. Xu, D. Qian, M. Z. Hasan, N. P. Ong, A. Yazdani, and R. J. Cava, Development of ferromagnetism in the doped topological insulator $Bi_{2-x}Mn_xTe_3$, Phys. Rev. B **81**, 195203 (2010).
[12] J. S. Dyck, C. Drašar, P. Lošťák, and C. Uher, Low-temperature ferromagnetic properties of the diluted magnetic semiconductor $Sb_{2-x}Cr_xTe_3$, Phys. Rev. B **71**, 115214 (2005).
[13] Z. Zhou, Y.-J. Chien, and C. Uher, Thin film dilute ferromagnetic semiconductors $Sb_{2-x}Cr_xTe_3$ with a Curie temperature up to 190 K, Phys. Rev. B **74**, 224418 (2006).
[14] J. S. Dyck, P. Hájek, P. Lošťák, and C. Uher, Diluted magnetic semiconductors based on $Sb_{2-x}V_xTe_3$ ($0.01 \leqslant x \leqslant 0.03$), Phys. Rev. B **65**, 115212 (2002).
[15] P. P. J. Haazen, J.-B. Laloe, T. J. Nummy, H. J. M. Swagten, P. Jarillo-Herrero, D. Heiman, and J. S. Moodera, Ferromagnetism in thin-film Cr-doped topological insulator Bi_2Se_3, Appl. Phys. Lett. **100**, 082404 (2012).
[16] L. B. Duffy, A. I. Figueroa, G. van der Laan, and T. Hesjedal, Codoping of Sb_2Te_3 thin films with V and Cr, Phys. Rev. Mater. **1**, 064409 (2017).

[17] X.-L. Qi, T. L. Hughes, and S.-C. Zhang, Topological field theory of time-reversal invariant insulators, Phys. Rev. B **78**, 195424 (2008).

[18] C. X. Liu, X. L. Qi, X. Dai, Z. Fang, and S. C. Zhang, Quantum Anomalous Hall Effect in $Hg_{1-y}Mn_yTe$ Quantum Wells, Phys. Rev. Lett. **101**, 146802 (2008).

[19] R. Yu, W. Zhang, H.-J. Zhang, S.-C. Zhang, X. Dai, and Z. Fang, Quantized anomalous Hall effect in magnetic topological insulators, Science **329**, 61 (2010).

[20] X.-L. Qi, R. Li, J. Zang, and S.-C. Zhang, Inducing a magnetic monopole with topological surface states, Science **323**, 1184 (2009).

[21] W.-K. Tse and A. H. MacDonald, Giant Magneto-Optical Kerr Effect and Universal Faraday Effect in Thin-Film Topological Insulators, Phys. Rev. Lett. **105**, 057401 (2010).

[22] T. Fujita, M. B. A. Jalil, and S. G. Tan, Topological Insulator Cell for Memory and Magnetic Sensor Applications, Appl. Phys. Express **4**, 094201 (2011).

[23] D. A. Abanin and D. A. Pesin, Ordering of Magnetic Impurities and Tunable Electronic Properties of Topological Insulators, Phys. Rev. Lett. **106**, 136802 (2011).

[24] C.-Z. Chang, J. Zhang, X. Feng, J. Shen, Z. Zhang, M. Guo, K. Li, Y. Ou, P. Wei, L.-L. Wang, Z.-Q. Ji, Y. Feng, S. Ji, X. Chen, J. Jia, X. Dai, Z. Fang, S.-C. Zhang, K. He, Y. Wang *et al.*, Experimental observation of the quantum anomalous Hall effect in a magnetic topological insulator, Science **340**, 167 (2013).

[25] S. Oh, The Complete Quantum Hall Trio, Science **340**, 153 (2013).

[26] J. G. Checkelsky, R. Yoshimi, A. Tsukazaki, K. S. Takahashi, Y. Kozuka, J. Falson, M. Kawasaki, and Y. Tokura, Trajectory of the anomalous Hall effect towards the quantized state in a ferromagnetic topological insulator, Nat. Phys. **10**, 731 (2014).

[27] X. Kou, S.-T. Guo, Y. Fan, L. Pan, M. Lang, Y. Jiang, Q. Shao, T. Nie, K. Murata, J. Tang, Y. Wang, L. He, T.-K. Lee, W.-L. Lee, and K. L. Wang, Scale-Invariant Quantum Anomalous Hall Effect in Magnetic Topological Insulators beyond the Two-Dimensional Limit, Phys. Rev. Lett. **113**, 137201 (2014).

[28] C.-Z. Chang, W. Zhao, D. Y. Kim, H. Zhang, B. A. Assaf, D. Heiman, S.-C. Zhang, C. Liu, M. H. W. Chan, and J. S. Moodera, High-precision realization of robust quantum anomalous Hall state in a hard ferromagnetic topological insulator, Nat. Mater. **14**, 473 (2015).

[29] G. Wang, X. Zhu, J. Wen, X. Chen, K. He, L. Wang, X. Ma, Y. Liu, X. Dai, Z. Fang, J. Jia, and Q. Xue, Atomically smooth ultrathin films of topological insulator Sb_2Te_3, Nano Res. **3**, 874 (2010).

[30] Y. Iwata, H. Kobayashi, S. Kikuchi, E. Hatta, and K. Mukasa, In situ reflection high-energy electron diffraction (RHEED) observation of Bi_2Te_3/Sb_2Te_3 multilayer film growth, J. Cryst. Growth **203**, 125 (1999).

[31] Y.-J. Chien, Z. Zhou, and C. Uher, Growth and transport properties of $Sb_{2-x}V_xTe_3$ thin films on sapphire substrates, J. Cryst. Growth **283**, 309 (2005).

[32] R. Venkatasubramanian, T. Colpitts, E. Watko, M. Lamvik, and N. ElMasry, MOCVD of Bi_2Te_3, Sb_2Te_3 and their superlattice structures for thin-film thermoelectric applications, J. Cryst. Growth **170**, 817 (1997).

[33] G. Simon and W. Y. Eichler, Galvanomagnetische und thermoelektrische transportuntersuchungen an Sb_2Te_3, Phys. Status Solidi B **103**, 289 (1981).

[34] R. Venkatasubramanian, E. Siivola, T. Colpitts, and B. O'Quinn, Thin-film thermoelectric devices with high room temperature figures of merit, Nature (London) **413**, 597 (2001).

[35] D. Hsieh, Y. Xia, D. Qian, L. Wray, F. Meier, J. H. Dil, J. Osterwalder, L. Patthey, A. V. Fedorov, H. Lin, A. Bansil, D. Grauer, Y. S. Hor, R. J. Cava, and M. Z. Hasan, Observation of Time-Reversal-Protected Single-Dirac-Cone Topological-Insulator States in Bi_2Te_3 and Sb_2Te_3, Phys. Rev. Lett. **103**, 146401 (2009).

[36] Z. H. Zhou, Y. J. Chien, and C. Uher, Thin-film ferromagnetic semiconductors based on $Sb_{2-x}V_xTe_3$ with T_C of 177 K, Appl. Phys. Lett. **87**, 112503 (2005).

[37] S. E. Harrison, L. J. Collins-McIntyre, S. Li, A. A. Baker, L. R. Shelford, Y. Huo, A. Pushp, S. S. P. Parkin, J. S. Harris, E. Arenholz, G. van der Laan, and T. Hesjedal, Study of Gd-doped Bi_2Te_3 thin films: Molecular beam epitaxy growth and magnetic properties, J. Appl. Phys. **115**, 023904 (2014).

[38] L. B. Duffy, N.-J. Steinke, J. A. Krieger, A. I. Figueroa, K. Kummer, T. Lancaster, S. R. Giblin, F. L. Pratt, S. J. Blundell, T. Prokscha, A. Suter, S. Langridge, V. N. Strocov, Z. Salman, G. van der Laan, and T. Hesjedal, Microscopic effects of Dy doping in the topological insulator Bi_2Te_3, Phys. Rev. B **97**, 174427 (2018).

[39] L. B. Duffy, A. I. Figueroa, L. Gładczuk, N.-J. Steinke, K. Kummer, G. van der Laan, and T. Hesjedal, Magnetic proximity coupling to Cr-doped Sb_2Te_3 thin films, Phys. Rev. B **95**, 224422 (2017).

[40] L. B. Duffy, A. Frisk, D. M. Burn, N.-J. Steinke, J. Herrero-Martin, A. Ernst, G. van der Laan, and T. Hesjedal, Imposing long-range ferromagnetic order in rare-earth-doped magnetic topological-insulator heterostructures, Phys. Rev. Mater. **2**, 054201 (2018).

[41] L. B. Duffy, N. J. Steinke, D. M. Burn, A. Frisk, L. Lari, B. Kuerbanjiang, V. K. Lazarov, G. van der Laan, S. Langridge, and T. Hesjedal, Magnetic profile of proximity-coupled $(Dy, Bi)_2Te_3/(Cr, Sb)_2Te_3$ topological insulator heterostructures, Phys. Rev. B **100**, 054402 (2019).

[42] A. I. Figueroa, T. Hesjedal, and N.-J. Steinke, Magnetic order in 3D topological insulators: Wishful thinking or gateway to emergent quantum effects? Appl. Phys. Lett. **117**, 150502 (2020).

[43] K. Lai, W. Kundhikanjana, M. A. Kelly, Z.-X. Shen, J. Shabani, and M. Shayegan, Imaging of Coulomb-Driven Quantum Hall Edge States, Phys. Rev. Lett. **107**, 176809 (2011).

[44] K. C. Nowack, E. M. Spanton, M. Baenninger, M. Koenig, J. R. Kirtley, B. Kalisky, C. Ames, P. Leubner, C. Bruene, H. Buhmann, L. W. Molenkamp, D. Goldhaber-Gordon, and K. A. Moler, Imaging currents in HgTe quantum wells in the quantum spin Hall regime, Nat. Mater. **12**, 787 (2013).

[45] E. M. Spanton, K. C. Nowack, L. Du, G. Sullivan, R.-R. Du, and K. A. Moler, Images of Edge Current in InAs/GaSb Quantum Wells, Phys. Rev. Lett. **113**, 026804 (2014).

[46] I. Lee, C. K. Kim, J. Lee, S. J. L. Billinge, R. Zhong, J. A. Schneeloch, T. Liu, T. Valla, J. M. Tranquada, G. Gu, and J. C. S. Davis, Imaging Dirac-mass disorder from magnetic dopant atoms in the ferromagnetic topological insulator $Cr_x(Bi_{0.1}Sb_{0.9})_{2-x}Te_3$, Proc. Natl. Acad. Sci. USA **112**, 1316 (2015).

[47] W. Wang, F. Yang, C. Gao, J. Jia, G. D. Gu, and W. Wu, Visualizing ferromagnetic domains in magnetic topological insulators, APL Mater. **3**, 083301 (2015).

[48] W. Wang, C.-Z. Chang, J. S. Moodera, and W. Wu, Visualizing ferromagnetic domain behavior of magnetic topological insulator thin films, npj Quant. Mater. **1**, 16023 (2016).

[49] A. Singh, V. S. Kamboj, J. Liu, J. Llandro, L. B. Duffy, S. P. Senanayak, H. E. Beere, A. Ionescu, D. A. Ritchie, T. Hesjedal, and C. H. W. Barnes, Systematic study of ferromagnetism in $Cr_xSb_{2-x}Te_3$ topological insulator thin films using electrical and optical techniques, Sci. Rep. **8**, 17024 (2018).

[50] S. Gupta, S. Kanai, F. Matsukura, and H. Ohno, Magnetic and transport properties of Sb_2Te_3 doped with high concentration of Cr, Appl. Phys. Express **10**, 103001 (2017).

[51] L. J. Collins-McIntyre, L. B. Duffy, A. Singh, N.-J. Steinke, C. J. Kinane, T. R. Charlton, A. Pushp, A. J. Kellock, S. S. P. Parkin, S. N. Holmes, C. H. W. Barnes, G. van der Laan, S. Langridge, and T. Hesjedal, Structural, electronic, and magnetic investigation of magnetic ordering in MBE-grown $Cr_xSb_{2-x}Te_3$ thin films, Europhys. Lett. **115**, 27006 (2016).

[52] A. I. Figueroa, G. van der Laan, L. J. Collins-McIntyre, S.-L. Zhang, A. A. Baker, S. E. Harrison, P. Schönherr, G. Cibin, and T. Hesjedal, Magnetic Cr doping of Bi_2Se_3: Evidence for divalent Cr from x-ray spectroscopy, Phys. Rev. B **90**, 134402 (2014).

[53] V. S. Kamboj, A. Singh, L. Jakob, L. B. Duffy, N. Idros, S. P. Senanayak, A. Ionescu, H. E. Beere, C. H. W. Barnes, T. Hesjedal, and D. A. Ritchie, Temperature dependence of the ferromagnetic response in $Cr_xSb_{2-x}Te_3$ topological insulator thin films investigated using terahertz spectroscopy and magneto-transport, in *Terahertz, RF, Millimeter, and Submillimeter-Wave Technology and Applications XII*, Vol. 10917, edited by L. P. Sadwick and T. Yang (SPIE, Bellingham, WA, 2019), pp. 263–271

[54] B. Li, Q. Fan, F. Ji, Z. Liu, H. Pan, and S. Qiao, Carrier dependent ferromagnetism in chromium doped topological insulator $Cr_y(Bi_xSb_{1-x})_{2-y}Te_3$, Phys. Lett. A **377**, 1925 (2013).

[55] Q. Liu, C.-X. Liu, C. Xu, X.-L. Qi, and S.-C. Zhang, Magnetic Impurities on the Surface of a Topological Insulator, Phys. Rev. Lett. **102**, 156603 (2009).

[56] J. Stöhr, Exploring the microscopic origin of magnetic anisotropies with x-ray magnetic circular dichroism (XMCD) spectroscopy, J. Magn. Magn. Mater. **200**, 470 (1999).

[57] G. van der Laan, Applications of soft X-ray magnetic dichroism, J. Phys.: Conf. Ser. **430**, 012127 (2013).

[58] G. van der Laan and A. I. Figueroa, X-ray magnetic circular dichroism: A versatile tool to study magnetism, Coord. Chem. Rev. **277–278**, 95 (2014).

[59] J. Stöhr, H. Padmore, S. Anders, T. Stammler, and M. Scheinfein, Principles of X-ray magnetic dichroism spectromicroscopy, Surf. Rev. Lett. **05**, 1297 (1998).

[60] O. Sandig, J. Herrero-Albillos, F. M. Römer, N. Friedenberger, J. Kurde, T. Noll, M. Farle, and F. Kronast, Imaging magnetic responses of nanomagnets by XPEEM, J. Electron Spectrosc. Relat. Phenom. **185**, 365 (2012).

[61] C. M. Schneider and G. Schönhense, Investigating surface magnetism by means of photoexcitation electron emission microscopy, Rep. Prog. Phys. **65**, 1785 (2002).

[62] S. Zhang, F. Kronast, G. van der Laan, and T. Hesjedal, Real-space observation of skyrmionium in a ferromagnet-magnetic topological insulator heterostructure, Nano Lett. **18**, 1057 (2018).

[63] A. I. Figueroa, G. van der Laan, S. E. Harrison, G. Cibin, and T. Hesjedal, Oxidation effects in rare earth doped topological insulator thin films, Sci. Rep. **6**, 22935 (2016).

[64] K. Virwani, S. E. Harrison, A. Pushp, T. Topuria, E. Delenia, P. Rice, A. Kellock, L. Collins-McIntyre, J. Harris, T. Hesjedal, and S. Parkin, Controlled removal of amorphous Se capping layer from a topological insulator, Appl. Phys. Lett. **105**, 241605 (2014).

[65] T. Prokscha, E. Morenzoni, K. Deiters, F. Foroughi, D. George, R. Kobler, A. Suter, and V. Vrankovic, The new μE4 beam at PSI: A hybrid-type large acceptance channel for the generation of a high intensity surface-muon beam, Nucl. Instrum. Methods Phys. Res., Sect. A **595**, 317 (2008).

[66] J. P. Biersack and W. Eckstein, Sputtering studies with the Monte Carlo Program TRIM.SP, Appl. Phys. A **34**, 73 (1984).

[67] J. A. Krieger, C.-Z. Chang, M.-A. Husanu, D. Sostina, A. Ernst, M. M. Otrokov, T. Prokscha, T. Schmitt, A. Suter, M. G. Vergniory, E. V. Chulkov, J. S. Moodera, V. N. Strocov, and Z. Salman, Spectroscopic perspective on the interplay between electronic and magnetic properties of magnetically doped topological insulators, Phys. Rev. B **96**, 184402 (2017).

[68] J. A. Krieger, Y. Ou, M. Caputo, A. Chikina, M. Döbeli, M.-A. Husanu, I. Keren, T. Prokscha, A. Suter, C.-Z. Chang, J. S. Moodera, V. N. Strocov, and Z. Salman, Do topology and ferromagnetism cooperate at the EuS/Bi_2Se_3 interface? Phys. Rev. B **99**, 064423 (2019).

[69] A. A. Baker, A. I. Figueroa, K. Kummer, L. J. Collins-McIntyre, T. Hesjedal, and G. van der Laan, Magnetic proximity-enhanced Curie temperature of Cr-doped Bi_2Se_3 thin films, Phys. Rev. B **92**, 094420 (2015).

[70] M. Ye, W. Li, S. Zhu, Y. Takeda, Y. Saitoh, J. Wang, H. Pan, M. Nurmamat, K. Sumida, F. Ji, Z. Liu, H. Yang, Z. Liu, D. Shen, A. Kimura, S. Qiao, and X. Xie, Carrier-mediated ferromagnetism in the magnetic topological insulator Cr-doped $(Sb, Bi)_2Te_3$, Nat. Commun. **6**, 8913 (2015).

[71] D. M. Burn, L. B. Duffy, R. Fujita, S. L. Zhang, A. I. Figueroa, J. Herrero-Martin, G. van der Laan, and T. Hesjedal, Cr_2Te_3 Thin Films for Integration in Magnetic Topological Insulator Heterostructures, Sci. Rep. **9**, 10793 (2019).

[72] J. Dijkstra, H. H. Weitering, C. F. van Bruggen, C. Haas, and R. A. de Groot, Band-structure calculations, and magnetic and transport properties of ferromagnetic chromium tellurides (CrTe, Cr_3Te_4, Cr_2Te_3), J. Phys.: Condens. Matter **1**, 9141 (1989).

[73] K. Gas, A. Królicka, K. Dybko, P. Nowicki, Z. Khosravizadeh, T. Story, and M. Sawicki, Magnetic constitution of topologically trivial thermoelectric PbTe:Cr, J. Magn. Magn. Mater. **537**, 168154 (2021).

[74] L. Fang, Y. Jia, D. J. Miller, M. L. Latimer, Z. L. Xiao, U. Welp, G. W. Crabtree, and W.-K. Kwok, Catalyst-Free Growth of Millimeter-Long Topological Insulator Bi_2Se_3 Nanoribbons and the Observation of the pi-Berry Phase, Nano Lett. **12**, 6164 (2012).

[75] E. O. Lachman, A. F. Young, A. Richardella, J. Cuppens, H. R. Naren, Y. Anahory, A. Y. Meltzer, A. Kandala, S. Kempinger, Y. Myasoedov, M. E. Huber, N. Samarth, and E. Zeldov, Visualization of superparamagnetic dynamics in magnetic topological insulators, Sci. Adv. **1**, e1500740 (2015).

[76] L. J. Collins-McIntyre, S. E. Harrison, P. Schönherr, N.-J. Steinke, C. J. Kinane, T. R. Charlton, D. Alba-Veneroa, A. Pushp, A. J. Kellock, S. S. P. Parkin, J. S. Harris, S. Langridge, G. van der Laan, and T. Hesjedal, Magnetic ordering in Cr-doped Bi_2Se_3 thin films, Europhys. Lett. **107**, 57009 (2014).

[77] A. Tcakaev, V. B. Zabolotnyy, R. J. Green, T. R. F. Peixoto, F. Stier, M. Dettbarn, S. Schreyeck, M. Winnerlein, R. C. Vidal, S. Schatz, H. B. Vasili, M. Valvidares, K. Brunner, C. Gould, H. Bentmann, F. Reinert, L. W. Molenkamp, and V. Hinkov, Comparing magnetic ground-state properties of the V- and Cr-doped topological insulator $(Bi, Sb)_2Te_3$, Phys. Rev. B **101**, 045127 (2020).

[78] J. H. Van Vleck, Models of exchange coupling in ferromagnetic media, Rev. Mod. Phys. **25**, 220 (1953).

[79] M. Li, C. Z. Chang, L. Wu, J. Tao, W. Zhao, M. H. W. Chan, J. S. Moodera, J. Li, and Y. Zhu, Experimental Verification of the Van Vleck Nature of Long-Range Ferromagnetic Order in the Vanadium-Doped Three-Dimensional Topological Insulator Sb_2Te_3, Phys. Rev. Lett. **114**, 146802 (2015).

[80] M. F. Islam, C. M. Canali, A. Pertsova, A. Balatsky, S. K. Mahatha, C. Carbone, A. Barla, K. A. Kokh, O. E. Tereshchenko, E. Jiménez, N. B. Brookes, P. Gargiani, M. Valvidares, S. Schatz, T. R. F. Peixoto, H. Bentmann, F. Reinert, J. Jung, T. Bathon, K. Fauth *et al.*, Systematics of electronic and magnetic properties in the transition metal doped Sb_2Te_3 quantum anomalous Hall platform, Phys. Rev. B **97**, 155429 (2018).

[81] M. G. Vergniory, M. M. Otrokov, D. Thonig, M. Hoffmann, I. V. Maznichenko, M. Geilhufe, X. Zubizarreta, S. Ostanin, A. Marmodoro, J. Henk, W. Hergert, I. Mertig, E. V. Chulkov, and A. Ernst, Exchange interaction and its tuning in magnetic binary chalcogenides, Phys. Rev. B **89**, 165202 (2014).

[82] M. Ye, T. Xu, G. Li, S. Qiao, Y. Takeda, Y. Saitoh, S. Y. Zhu, M. Nurmamat, K. Sumida, Y. Ishida, S. Shin, and A. Kimura, Negative Te spin polarization responsible for ferromagnetic order in the doped topological insulator $V_{0.04}(Sb_{1-x}Bi_x)_{1.96}Te_3$, Phys. Rev. B **99**, 144413 (2019).

[83] C. Śliwa, C. Autieri, J. A. Majewski, and T. Dietl, Superexchange dominates in magnetic topological insulators, Phys. Rev. B **104**, L220404 (2021).

[84] T. Dietl, H. Ohno, F. Matsukura, J. Cibert, and D. Ferrand, Zener model description of ferromagnetism in zinc-blende magnetic semiconductors, Science **287**, 1019 (2000).

[85] V. G. Storchak, D. G. Eshchenko, E. Morenzoni, T. Prokscha, A. Suter, X. Liu, and J. K. Furdyna, Spatially Resolved Inhomogeneous Ferromagnetism in (Ga,Mn)As Diluted Magnetic Semiconductors: A Microscopic Study by Muon Spin Relaxation, Phys. Rev. Lett. **101**, 027202 (2008).

[86] D. J. Priour and S. Das Sarma, Clustering in disordered ferromagnets: The Curie temperature in diluted magnetic semiconductors, Phys. Rev. B **73**, 165203 (2006).